PCCP

ROYAL SOCIETY OF CHEMISTRY

PAPER

View Article Online
View Journal | View Issue

Cite this: *Phys. Chem. Chem. Phys.*, 2026, **28**, 6636

Pressure- and aggregation-induced modulation of linear and nonlinear optical properties in a push–pull chromophore: insights from computational modelling

Josianne Owona,[abc] Selom J. Goto,[a] Lionel Truflandier,[a] Claire Tonnelé *[cd] and Frédéric Castet *[a]

We report a theoretical investigation of the structural and optical responses of a molecular crystal based on a push–pull chromophore subjected to increasing isotropic pressure ranging from 1 to 30 kbar. Geometry optimizations at the DFT level reveal pronounced changes in unit cell parameters, particularly along the stacking and charge-transfer directions, accompanied by significant volume compression, reaching 17% at the highest pressure. Pressure also alters key intramolecular torsional angles and intermolecular stacking geometries, with non-linear variations and discontinuities observed in the evolution of these parameters. Time-dependent DFT calculations on pressure-adapted geometries of molecular dimers show that these structural changes lead to abrupt shifts in excited-state energies, oscillator strengths, exciton localization, and charge-transfer character. The external pressure is also shown to strongly influence the second-harmonic generation (SHG) response of the dimers, which are considered representative of the stacking arrangements in thin films. As rationalized using a truncated sum-over-states (SOS) approach, the pressure-induced variation in the SHG response is closely linked to changes in the charge-transfer character and absorption strength of a small set of low-lying excited states. Overall, our calculations indicate that increasing the external pressure from 1 to 30 kbar leads to an 11% decrease in the static first hyperpolarizability of the dimer. The dynamic first hyperpolarizability computed at an incident wavelength of 800 nm evolves non-monotonically with pressure, exhibiting a maximum around 8 kbar due to resonance effects at the second harmonic and an overall reduction of 74% from 1 to 30 kbar. These results suggest that external pressure provides an effective means to modulate the nonlinear optical properties of 2D materials based on these push–pull chromophores.

Received 20th October 2025,
Accepted 6th February 2026

DOI: 10.1039/d5cp04030b

rsc.li/pccp

Introduction

Responsive materials whose optical responses can be reversibly tuned by external stimuli are of considerable interest for modern photonics and optoelectronics.[1–4] Among them, nonlinear optical (NLO) materials play a central role, underpinning key technologies such as frequency conversion, optical signal processing, electro-optic modulation, optical switching, and high-density data storage. Organic materials based on π-conjugated chromophores are especially promising in this context, owing to their large optical nonlinearities, structural versatility, and the strong sensitivity of their electronic properties to changes in molecular conformation, packing, and intermolecular interactions.[5–13]

Among the various external stimuli that can be exploited, mechanical pressure offers a direct and powerful means to modulate these interactions in the solid state. Controlling the optical properties of organic solids based on π-conjugated chromophores through the application of external pressure is indeed crucial for a wide range of advanced applications, including mechanically responsive optoelectronic and photonic materials, pressure-sensitive sensors, stress-controlled optical modulation schemes and energy-harvesting systems.[14–19] In this context, mechanochromic and mechanofluorochromic materials, exhibiting changes in absorption and emission properties, respectively, in response to mechanical stimuli such as grinding, pressing, shearing and stretching, have attracted considerable interest.[20] Recent examples include donor–acceptor type fluorophores such as phenylenevinylene oligomers,[21,22]

[a] *Univ. Bordeaux, CNRS, Bordeaux INP, Institut des Sciences Moléculaires, UMR 5255, F-33400 Talence, France. E-mail: frederic.castet@u-bordeaux.fr*
[b] *Euskal Herriko Unibertsitatea, PK 1072, 20080 Donostia, Euskadi, Spain*
[c] *Donostia International Physics Center, 20018 Donostia, Euskadi, Spain. E-mail: claire.tonnele@dipc.org*
[d] *IKERBASQUE – Basque Foundation for Science, 48009 Bilbo, Euskadi, Spain*

diphenylamine[23] and triphenylamine[24] derivatives, organoboron complexes,[25,26] carbazole-based conjugates,[27] molecular co-crystals,[28] diketopyrrolopyrrole-based materials,[29] and pyridylvinylanthracene-based compounds,[30,31] which exhibit pronounced and reversible mechanoresponsive optical behaviour driven by changes in molecular packing or π–π interactions.

Going beyond linear optical responses, NLO properties such as second harmonic generation (SHG) of organic solids can also be tuned by mechanical stimuli, spanning stress-driven mechanochromic NLO materials and hydrostatic pressure-tunable NLO systems. Recent studies have shown that mechanical damage and deformation can have a direct impact on NLO responses in organic crystals. For instance, mechanical fracturing of self-healing organic NLO crystals based on dibenzoate derivatives leads to a decrease in SHG intensity at crack sites, with SHG intensity being restored after healing.[32] Mechanical bending or twisting can also largely modify the SHG intensity in flexible molecular crystals.[33–35] Regarding pressure-tunable NLO materials, early studies by Drickamer *et al.* demonstrated that phase transition triggered by hydrostatic compression in organic crystals is accompanied by significant variations in the SHG intensity.[36,37] Pressure-induced conformational changes in weakly hydrogen-bonded molecular crystals, arising from the collapse of supramolecular frameworks, have been shown to significantly modify the SHG efficiency.[38] Amino acids such as sarcosine, which has shown potential for NLO applications, exhibit large variations in their optical properties under hydrostatic pressure.[39] In organic–inorganic systems such as hybrid perovskites, compression has been shown to enhance organic–inorganic interactions and induce structural distortions, leading to a substantial increase in SHG intensity.[40] Furthermore, SHG has been employed as a sensitive probe of pressure-induced structural ordering in thin films.[41]

In this context, Roncali and coworkers reported, over a decade ago, the NLO mechanochromic behaviour of a material based on a push–pull chromophore.[42] This chromophore features a diphenylamine (DPA) donor unit *N*-substituted with an oligo-oxyethylene chain, linked *via* a thienyl (Th) π-conjugated spacer to a dicyanovinyl (DCV) acceptor group (Fig. 1b). In the crystalline state, both head-to-tail and face-to-face molecular arrangements were observed. Notably, thin-film interfaces of this compound, presumed to retain the non-centrosymmetric face-to-face aggregation found in the crystal, were shown to generate a SHG signal under 800 nm laser excitation. The disappearance of this NLO response upon mechanical smearing of the film suggested that SHG originates from ordered crystalline domains and that mechanical disruption of the local non-centrosymmetric structure leads to extinction of the SHG signal. This interpretation was further supported by thermal annealing experiments: annealing temporarily suppressed the SHG signal, which gradually reappeared after approximately 30 minutes under ambient conditions, indicating a reorganization toward the original molecular packing.

In this work, we present a computational study aimed at providing deeper insight into the role of molecular aggregation and of external mechanical stress in the linear and nonlinear optical responses of this material, hereafter referred to as DPA-Th-DCV. Our computational strategy relies on the combined use of periodic density functional theory (DFT) to model the crystal structure under increasing isotropic pressure (from 1 to 30 kbar) and time-dependent (TD) DFT calculations to evaluate the associated linear and nonlinear optical responses. This

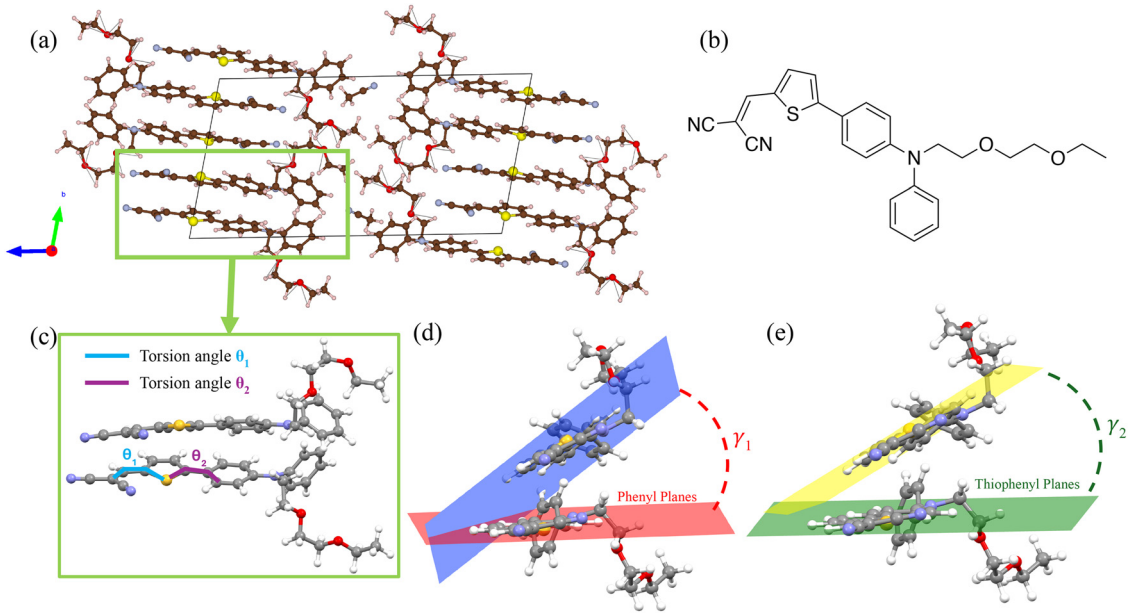

Fig. 1 Top: Scheme of the optimized crystal structure (a) and chemical structure of DPA-Th-DCV (b). Bottom: Molecular dimer (c) extracted from the unit cell for subsequent calculations of the optical properties. The torsion angles θ_1 and θ_2 discussed in the text are also defined. Angles between the planes of the phenyl rings (γ_1) (d) and between the planes of the thiophenyl rings (γ_2) (e) of the two monomers.

approach allows for the rationalization of the evolution of the optical properties based on the impact of an applied mechanical constraint on the geometry and spatial organisation of the molecular units within the crystal. The results demonstrate how fine-tuning of intermolecular interactions through pressure offers a viable strategy for the controlled modulation of the optical properties in this push–pull system.

Computational methods

Geometry optimizations and calculation of molecular optical properties

Geometry optimizations of DPA-Th-DCV conformers were carried out using DFT with the Gaussian 16 program,[43] using the CAM-B3LYP[44] exchange–correlation functional (XCF) with the Grimme D3 empirical dispersion correction[45] and the 6-311G(d) basis set. Molecular structures were confirmed to be real minima on the potential surface by the subsequent computation of harmonic vibrational frequencies and the absence of imaginary values. The vertical excitation energies and oscillator strengths associated with the low-lying excited states, as well as the components of the first hyperpolarizability tensor, were computed using TD-DFT at the same CAM-B3LYP-D3/6-311G(d) level of approximation. Linear optical properties were calculated both in the gas phase and, to compare with previously reported results,[42] in three solvents of increasing polarities: hexane (ε_0 = 1.88), dichloromethane (ε_0 = 8.93) and acetonitrile (ε_0 = 35.69). Solvation effects were simulated using the polarizable continuum model in its integral equation formalism (IEF-PCM).[46]

Optimization of crystal structures

Periodic DFT calculations were performed using the Quantum Espresso (QE) package[47,48] with the vdW-df2-c09 XCF, which was shown to accurately describe dispersion-bound van der Waals complexes.[31,49–51] The ultra-soft pseudopotential scheme was employed in all calculations, with pseudopotentials obtained from the standard solid-state pseudopotentials (SSSP) library.[52–54] The BFGS quasi-Newton algorithm was used with thresholds of 10^{-4} Ry Bohr^{-3} on all the atomic forces and 0.05 GPa (0.3×10^{-5} Ry Bohr^{-1}) on the largest component of the stress tensor when cell relaxation was applied. The bulk calculations were conducted using a regular $1 \times 1 \times 1$ k-point sampling of the first Brillouin zone. After standard testing, kinetic energy cut-offs of 70 Ry for the wave functions and 490 Ry for the augmentation charge density were adopted to achieve stable convergence of forces and stress. Self-consistent-field (SCF) convergence was achieved with a threshold of 10^{-6} Ry on the total energy. The QE calculations were pre- and post-processed using the atomic simulation environment (ASE).[55] The Mercury program[56] developed by the Cambridge Crystallographic Data Centre (CCDC), as well as the VESTA program,[57] were used for visualization and exploitation purposes. XRD crystal structures were used as starting guess for geometry optimizations, first without any external constraint to assess the reliability of the computational level and then upon applying increasing isotropic pressures (up to 30 kbar) to monitor the structural deformations induced by the mechanical stress. To eliminate the possibility of falling into a local minimum, optimizations under pressure were also carried out using the structure obtained at the next lower pressure as the initial guess; the resulting geometries were identical to those obtained when starting from the XRD structure. Note that the experimental crystallographic structure contains two acetonitrile molecules per unit cell, which could not be refined experimentally. Including these solvent molecules was essential to achieve convergence. The calculations converged towards the same structure regardless of their initial orientation.

Calculation of the excited states and optical properties of crystalline aggregates

As the non-centrosymmetric co-facial (or face-to-face) arrangement adopted by the molecules within the crystal was assumed by Roncali and coworkers[42] to provide a good description of the supramolecular organization in thin films, the associated dimers were extracted from the optimized unit cells (Fig. 1). Low-lying excited states and second-order NLO responses were then computed at the TD-DFT/CAM-B3LYP-D3/6-311G(d) level on these structures. The local or intermolecular charge transfer character (CT) of the excited states was further analysed using the TheoDORE toolbox, which uses the one-electron transition density matrix to decompose the excitation into different local and CT contributions.[58]

The first hyperpolarizability components (β_{ijk}) of monomers and dimers extracted from the optimized crystal structures were calculated in both the static limit and the dynamic (frequency dependent) regime of the second harmonic generation, using the experimental incident wavelength of 800 nm.[42] The components and norm of the first hyperpolarizability vector were then calculated as follows:

$$\beta_i = \frac{1}{3}\sum_j \left(\beta_{ijj} + \beta_{jij} + \beta_{jji}\right) \quad (1)$$

$$\beta = \sqrt{\left(\beta_x^2 + \beta_y^2 + \beta_z^2\right)} \quad (2)$$

where z is the charge transfer axis of the molecules. The anisotropy of the NLO response was also characterized as the ratio between the longitudinal and transverse components:

$$\alpha_\beta = \frac{|\beta_z|}{\sqrt{\beta_x^2 + \beta_y^2}} \quad (3)$$

Furthermore, the contributions of the low-lying electronic excited states (S_n) to the NLO responses were analyzed using the sum-over-states (SOS) expression of the first hyperpolarizability.[59–61] Although this scheme is known to overestimate hyperpolarizability values, especially truncated implementations, it has the advantage of expressing the NLO responses in terms of spectroscopic quantities, allowing for a qualitative understanding of the NLO properties.

According to this formalism, the general expression of the dynamic diagonal component β_{zzz} in the case of the SHG process reads

$$\beta_{zzz}^{\mathrm{SOS}}(-2\omega;\omega,\omega) = 2\sum_{n\neq 0}\sum_{m\neq 0}\left\{\frac{\mu_{0n}^{z}\left(\mu_{nm}^{z}-\mu_{00}^{z}\delta_{nm}\right)\mu_{m0}^{z}}{(\Delta E_{0n}-2\hbar\omega)(\Delta E_{0m}-\hbar\omega)} + \frac{\mu_{0n}^{z}\left(\mu_{nm}^{z}-\mu_{00}^{z}\delta_{nm}\right)\mu_{m0}^{z}}{(\Delta E_{0n}+\hbar\omega)(\Delta E_{0m}-\hbar\omega)} + \frac{\mu_{0n}^{z}\left(\mu_{nm}^{z}-\mu_{00}^{z}\delta_{nm}\right)\mu_{m0}^{z}}{(\Delta E_{0n}+\hbar\omega)(\Delta E_{0m}+2\hbar\omega)}\right\} \quad (4)$$

where μ_{0n}^{z} is the z-component of the transition dipole between the ground (S_0) and nth singlet excited state (S_n), μ_{nm}^{z} the z-component of the transition dipole moment between states S_n and S_m, μ_{00}^{z} the z-component of the ground state dipole moment, δ_{nm} the Kronecker delta function, and ΔE_{0n} the energy of the $S_0 \rightarrow S_n$ optical transition. For a dynamic NLO process, the denominators also depend on the energy of the incident laser field. For an incident wavelength of 800 nm, $\hbar\omega$ = 1.55 eV, while $\hbar\omega$ = 0 in the static limit. All quantities involved in eqn (4) were calculated at the TD-DFT level using Gaussian 16, except the μ_{nm}^{z} terms, which were obtained using the Multiwfn software.[62,63] More details on the SOS expressions are provided in the SI (Section 6). In the following, all β values are reported in atomic units (1 a.u. of $\beta = 3.63 \times 10^{-42}$ m^4 V^{-1} = 3.2063×10^{-53} C^3 m^3 J^{-2} = 8.641×10^{-33} esu), according to the T convention.[64]

The adopted computational scheme, in which the geometries of the DPA-Th-DCV dimers used in the NLO calculations are extracted from crystal-structure optimizations performed under periodic boundary conditions, captures pressure-dependent structural effects arising from intermolecular steric interactions; however, electrostatic interactions and mutual polarization effects are neglected in the computation of the NLO properties. To evaluate the importance of these missing contributions, calculations were carried out using the hybrid QM/MM ''own N-layered integrated molecular orbitals and molecular mechanics'' (ONIOM) approach,[65] in which the DPA-Th-DCV dimer constitutes the quantum-mechanical (QM) region, while the surrounding molecular units are treated classically in the molecular-mechanical (MM) region using the universal force field (see details in the SI, Section 5.1). The results, obtained for P = 0 and P = 30 kbar, indicate that the pressure-induced variations of the NLO properties are very similar, whether they are calculated for the isolated DPA-Th-DCV dimer or for the environment-embedded system. Consequently, environmental effects were not explicitly included in the final calculations. Furthermore, as shown in Table S18, the acetonitrile molecules present in the unit cell have a negligible impact on the pressure-induced variations of the NLO properties and were therefore also omitted from the calculations.

Results and discussion

Molecular electronic and optical properties

As presented in Table S1, DPA-Th-DCV possesses four quasi isoenergetic conformers differing by the orientation of the thiophenyl linker and the terminal DCV substituent. In all conformers, the thiophenyl and DCV groups are coplanar with $\theta_1 \sim 1^\circ$, while the thiophenyl and phenyl groups make an angle of $\theta_2 \sim 30^\circ$ (see Fig. 1 for the definition of the dihedral angles). In addition, all conformers display a significant charge transfer between the DPA donor and the DCV acceptor in their electronic ground-state, resulting in dipole moment values exceeding 10 D. The charge distributions within the different chemical fragments of the most stable conformer, calculated using the Mulliken and natural population analysis (NPA) approximations, are shown in Fig. S1. The π lone pair of the DPA nitrogen is partially delocalized, as indicated by the NPA electron orbital occupancy of 1.759. The π-electron conjugation is also reflected in the near-zero (0.026 Å) bond length alternation (BLA) along the conjugated bridge connecting the donor and acceptor groups. The UV-vis absorption spectra of DPA-Th-DCV in the gas phase and in different solvents, computed by weighting the spectrum of each stable conformer by its Boltzmann statistical population at room temperature (Table S1), show a first absorption band in the near-UV range and a second, more intense, in the visible domain (Fig. S2). The calculated spectra reproduce the overall shapes observed experimentally[42] and correctly show the absence of significant solvent effects, although the computed bands are systematically shifted towards higher energies. The $S_0 \rightarrow S_1$ absorption band results from a combination of HOMO $\rightarrow$ LUMO and HOMO−1 $\rightarrow$ LUMO (π–π*) electron excitations, with the former contributing the most (the numerical details are given in Tables S2–S5). As shown in Fig. 2, the HOMO is spread over the whole conjugated part of DPA-Th-DCV, while the LUMO is shifted towards the DCV acceptor, resulting in a significant intramolecular charge transfer (ICT) upon light absorption, as quantified by the large dipole moment variation between the S_0 and S_1 states (Table S6). The electron density variation map (Fig. 2) further illustrates

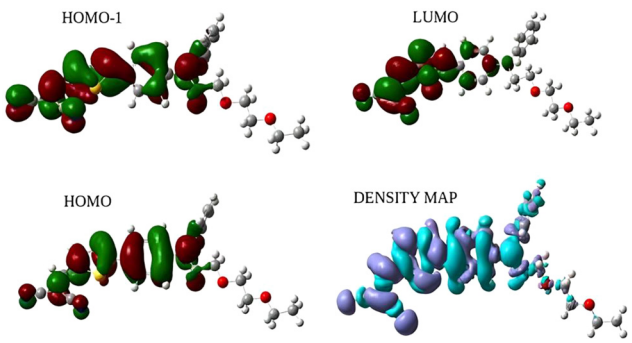

Fig. 2 Frontier molecular orbitals of DPA-Th-DCV and electron density variation involved in the $S_0 \rightarrow S_1$ vertical excitation. Dark (light) blue lobes in the density map are associated with an increase (decrease) in the electronic density. The calculations were performed at the TD-DFT/CAM-B3LYP-D3/6-311G(d) level.

the light-induced ICT from the DPA to the DCV group. It also shows that the oligo-oxyethylene chain does not contribute to the ICT, in accordance with the absence of delocalization of the MOs involved in the $S_0 \rightarrow S_1$ transition over this part of the molecule.

The static and dynamic components of the first hyperpolarizability vector for each conformer are reported in Table S7. Owing to the overall planar geometry of the molecule and its strongly dipolar character, the longitudinal contribution β_z, driven primarily by the β_{zzz} tensor component, dominates over the normal components, consistent with the internal charge transfer pathway being aligned along the *z*-axis (Table S7). This dipolar character of the NLO response is further evidenced by the unit sphere representation (USR)[66] of the β tensor, which provides a visual illustration of the symmetry of the second-order NLO response as a function of the molecular shape (Fig. S3). The large difference between the dynamic and static β vectors ($\beta_{dyn}/\beta_{stat} \sim 18$) highlights significant frequency dispersion effects, as expected from the high absorption intensity of the molecule at the second harmonic wavelength (400 nm). Additionally, the anisotropy factor exhibits a strong dependence on the conformer geometry in both regimes, indicating that it is highly sensitive to dynamic geometrical variations. However, such fluctuations are expected to be considerably constrained in the crystalline state.

Impact of mechanical strain on the crystal structure

The crystal geometry was first optimized without any external constraint. As shown in Table S8, the calculated lattice parameters show only slight differences with the experimental ones, validating the chosen computational level. The lattice parameters were thus computed using the same level of approximation under increasing isotropic pressures (Table S9). Their deviations with respect to the parameters optimized with no external pressure are presented in Fig. 3a and b. While the *a* cell edge remains quasi constant throughout the entire pressure range considered, the lengths of *b* and *c*, which are, respectively, aligned with the stacking axis and the ICT axis of the molecules (see Fig. 1), decrease steadily under mechanical stress, resulting in significant volume compression (Fig. 3c). The α angle between *b* and *c* cell edges decreases by 4.6° from 0 to 30 kbar, while the two other interaxial angles show less significant variation (<1°).

Pressure-induced variations in the geometric characteristics of molecular dimers extracted from the optimized unit cells were also monitored and are reported in Tables S10 and S11. Fig. 4a depicts the evolution with increasing pressure of the stacking angles γ_1 and γ_2 (see their definition in Fig. 1). The two angles decrease smoothly up to 9 kbar, indicating that the mean planes of the two monomers become increasingly parallel as the unit cell is compressed by the external mechanical stress. At 10 kbar, both angles drop abruptly (the evolution of γ_2 over the 0–10 kbar pressure range is illustrated in Fig. S4). Beyond this point, the evolution of the two angles differs: while γ_1 continues to decrease, γ_2 instead increases steadily with pressure. Another (smaller) discontinuity is observed at high pressure, around 27 kbar. Similar abrupt variations are found in the evolution of the intramolecular torsional angles θ_1 and θ_2. As discussed in the following sections, these structural changes alter the overall conjugation and the magnitude of the ICT within individual molecular units, thereby modulating both the linear and nonlinear optical responses of the aggregate. We also note that the θ_1 and θ_2 dihedral angles in the crystal at zero external pressure (θ_1 = 9.7° and −0.5° and θ_2 = 4.0° and −5.3° for monomers 1 and 2, respectively) differ significantly from those of the isolated molecule (θ_1 = −1.4° and θ_2 = −29.4°, see Table S1), highlighting the influence of crystalline confinement on the molecular geometry. In particular, molecules in the crystal adopt a more planar conformation, which favors π-electron conjugation and contributes to the observed spectral redshift compared to the isolated molecule, as discussed below.

To further characterize the evolution of intermolecular interactions with pressure, we resorted to the non-covalent interactions (NCI) method.[67,68] This approach uses the promolecular density $\rho(r)$ for the determination of the reduced density gradient scalar field (RDG, $s(\rho)$) and the sign of the second eigenvalue of the Hessian density matrix (λ_2) to determine the attractive or repulsive nature of the interactions. Moreover, the NCI results can be interpreted semi-quantitatively by calculating the interaction volume (Ω_{NCI}). Fig. 5a and b show the RDG and a three-dimensional view of the interaction regions between the molecules within the dimer taken at *P* = 0 kbar (see Fig. S5 for equivalent representations at higher pressures).

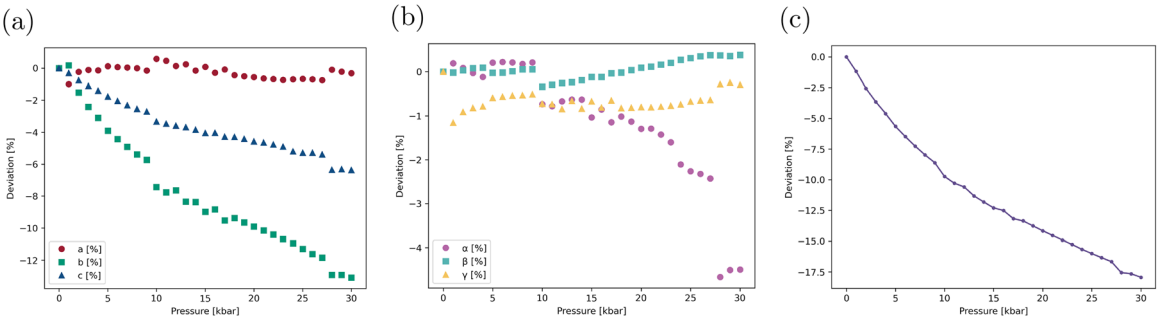

Fig. 3 Evolution of the unit cell parameters *a*, *b* and *c* (a), of the interaxial angles (b) and of the unit cell volume (c) with external pressure (% deviation with respect to the parameters optimized without external pressure).

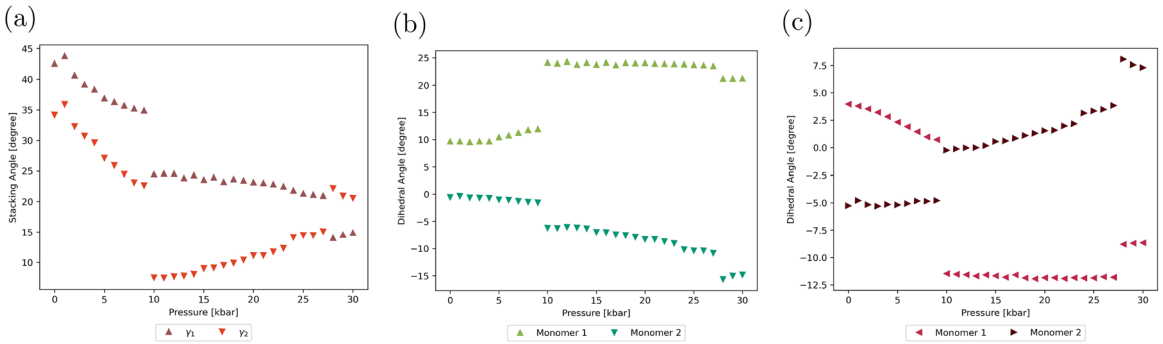

Fig. 4 Evolution of the stacking angles γ_1 and γ_2 (a) and of the molecular torsional angles θ_1 (b) and θ_2 (c) with external pressure. See Fig. 1 for the definition of the angles.

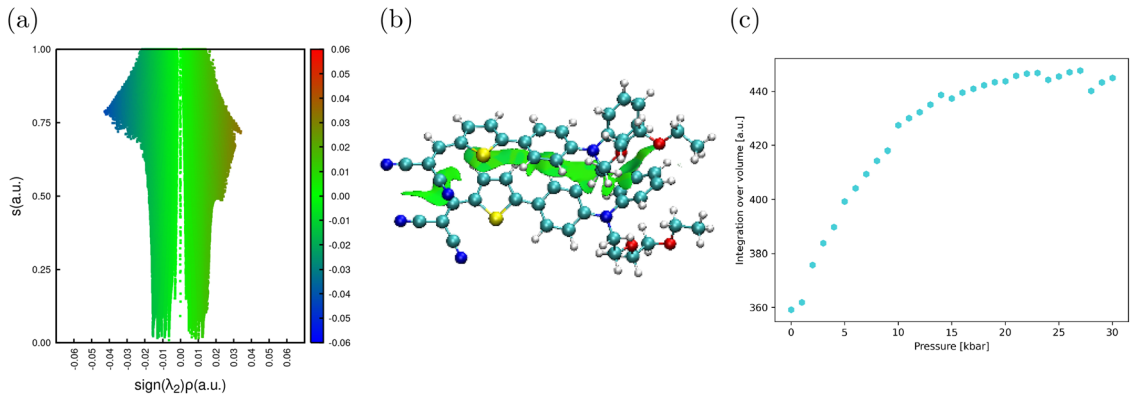

Fig. 5 (a) Reduced density gradient $s(\rho)$ *versus* $\mathrm{sign}(\lambda_2)\rho$ at P = 0 kbar, where the colour scheme goes from blue for strong attractive interactions to red for strong repulsive interactions, passing through green for weak van der Waals interactions; (b) NCI regions in the molecular dimer at P = 0 kbar; (c) evolution of the interaction volume Ω_{NCI} with pressure.

As expected, all intermolecular interactions are dominantly of the weak van der Waals type, with the majority occurring between the conjugated backbones of the molecules. The evolution of Ω_{NCI} with pressure (Fig. 5c) shows that the volume of NCI interactions progressively increases (up to 25%) as the unit cell is compressed and reaches a plateau at about 20 kbar.

Impact of mechanical strain on the linear optical properties

Fig. 6 displays the nature of the first four singlet excited states (S_1–S_4) of the dimer at zero external pressure, showing the main contributing electronic excitations and the associated molecular orbitals, all of which remain fully localized on individual molecular units. The $S_0 \rightarrow S_1$ transition is computed at 2.71 eV and exhibits a very low oscillator strength (f_{01} = 0.043), consistent with Kasha's model for H-aggregates. This transition is primarily composed of HOMO−1 → LUMO and HOMO → LUMO+1 excitations, indicating its intramolecular character. In contrast, the $S_0 \rightarrow S_2$ and $S_0 \rightarrow S_3$ transitions, located at 3.00 eV and 3.06 eV, respectively, exhibit high oscillator strengths (f_{02} = 1.414 and f_{03} = 0.797) and involve a significant HOMO → LUMO contribution, suggesting a partial intermolecular charge transfer nature. Finally, the S_4 state at 3.42 eV is a dark (f_{02} = 0.020) intermolecular CT state.

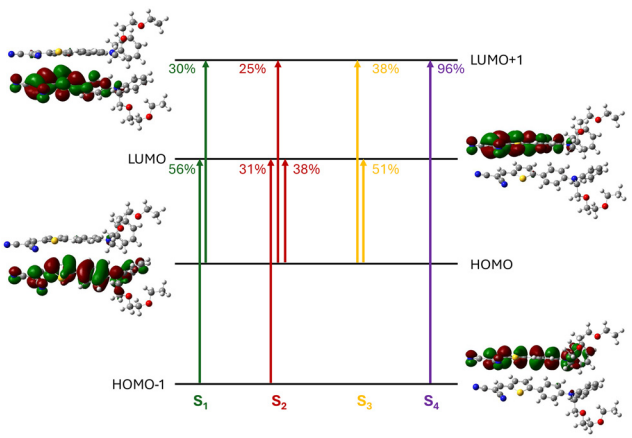

Fig. 6 Molecular orbitals and contributions (in %) of the main electronic excitations involved in the first four excited singlet states of the dimer with no external pressure. Only contributions >10% are reported.

The pressure-dependent evolution of the vertical transition energies and oscillator strengths associated with the S_1–S_4 states is reported in Table S12 and Fig. 7. As expected, the discontinuities observed in the evolution of the dihedral angles

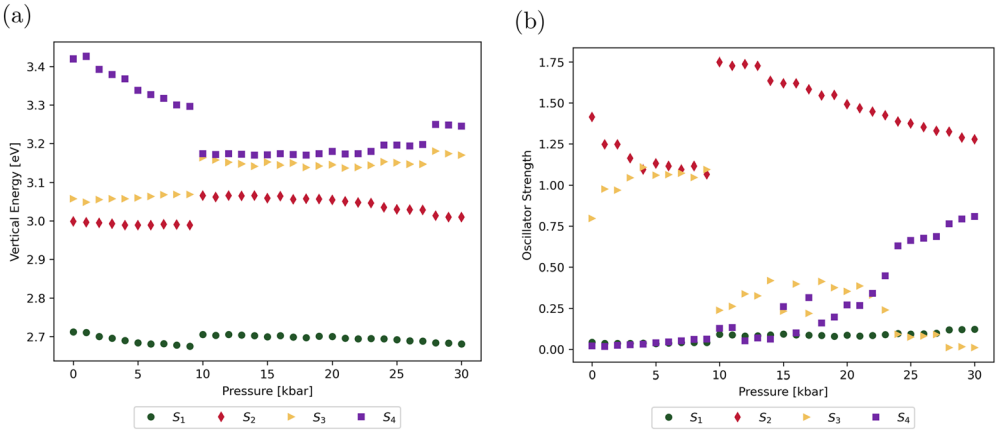

Fig. 7 Pressure-dependent evolution of the energies (a) and oscillator strengths (b) associated with the optical transitions towards the four first excited singlet states of the dimer.

around 10 and 27 kbar (Fig. 4) are reflected in the evolution of the optical properties, with each state being altered differently. The energy and oscillator strength of the (dark) $S_0 \rightarrow S_1$ transition remain nearly constant across the entire pressure range, indicating that this transition is not affected by the structural changes induced by external mechanical strain. At low external pressures (0–9 kbar), the energy of the $S_0 \rightarrow S_2$ transition is virtually unchanged, while the associated oscillator strength gradually decreases from 1.4 to 1.1. At 10 kbar, both the transition energy and oscillator strength exhibit a sharp increase, followed by a gradual decline as pressure is further raised. The transition energy towards the S_3 state follows a similar evolution with a discontinuity at 10 kbar. However, in contrast to the trend observed for the $S_0 \rightarrow S_2$ transition, the intensity of the $S_0 \rightarrow S_3$ transition dramatically drops at 10 kbar, with the oscillator strength decreasing from 1.095 to 0.238. Beyond this point, it fluctuates and eventually vanishes at the highest pressures. Finally, the $S_0 \rightarrow S_4$ transition, which is dark in the absence of external pressure, exhibits a gradual decrease in energy up to the structural discontinuity, after which it remains almost constant. Meanwhile, the corresponding oscillator strength increases from 15 kbar onward, reaching a substantial value of $\sim$0.8 at higher pressures.

The results reported in Fig. 7 show that, while the structural changes induced by isotropic pressure only have a modest impact on the optical properties within the 0–9 kbar range, they significantly alter the singlet state manifold at higher pressures, in terms of both transition energies and absorption intensities. In order to gain a deeper insight into the topology of the excited states, excitations were decomposed into local (intramolecular) and intermolecular CT contributions using the TheoDORE toolbox.[58] Electron–hole correlation plots for the S_1–S_4 excited states of the dimer are displayed in Fig. S6, while the pressure-induced evolution of their respective CT character is depicted in Fig. 8, together with the associated exciton size (see Tables S13 and S14 for numerical data). The nature of the excited states at key pressures (P = 0, 10 and 30 kbar) is further illustrated by the variation of the electron density upon excitation towards the S_1–S_4 states, as well as the corresponding charge transfer vectors, following the procedure proposed by Le Bahers and coworkers[69,70] (Fig. S7 and S8).

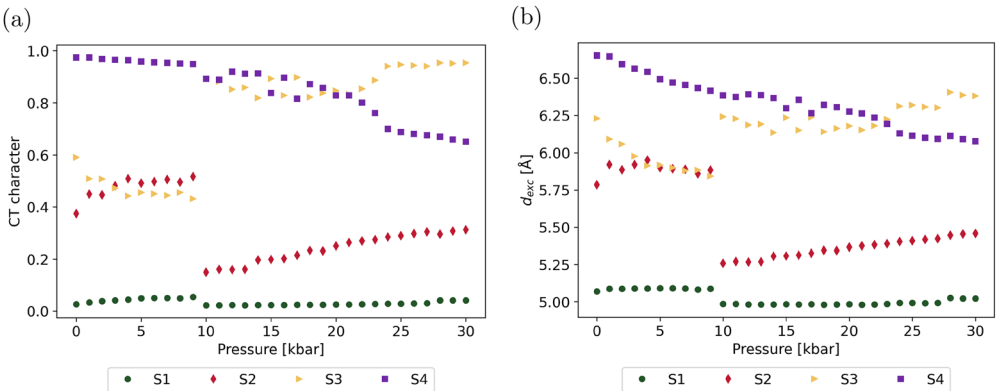

Fig. 8 Pressure-induced evolution of the intermolecular charge transfer character (a) and of the exciton size (b) in the S_1–S_4 excited states.

At zero external pressure, the $S_0 \rightarrow S_1$ transition is purely local in nature and corresponds to intramolecular excitations on both monomers, as expected from the MO contributions shown in Fig. 6. This local character is conserved at all pressures, with the intermolecular CT contribution remaining below 5%. The exciton size of about 5 Å reflects an intramolecular CT from the donor to the acceptor moiety within the two monomers, as confirmed by the charge transfer vector parallel to the conjugation axis of the molecules. In contrast, the S_2 state displays a partial intermolecular CT character of 37% at zero pressure and a larger exciton size (5.8 Å). The CT character gradually increases to 52% and then abruptly drops to 15% at P = 10 kbar, before rising smoothly again to reach 31% at P = 30 kbar. Analysis of the electron–hole correlation plots reveals that the CT character of S_2 observed before the structural transition corresponds to a charge transfer from monomer **1** to monomer **2**. In contrast, the exciton becomes more localized on monomer **1** after the discontinuity, as also illustrated by the density variation maps and CT vectors in Fig. S7 and S8. The abrupt decrease of the CT character of S_2 at 10 kbar aligns with the decrease of the exciton size from 5.9 to 5.3 Å, as well as with a larger absorption intensity, as indicated by the evolution of the oscillator strength of the $S_0 \rightarrow S_2$ transition (Fig. 7). The S_3 state evolves symmetrically to S_2, starting with a dominant CT character (59%) at zero pressure, corresponding to a charge transfer from monomer **1** to monomer **2** with an exciton size of 6.2 Å. This CT character gradually decreases up to the structural transition at 10 kbar, before rising abruptly to reach a quasi-pure CT character (89%), corresponding to a charge transfer from monomer **2** to monomer **1**. Here as well, the abrupt variation of the CT character of S_3 aligns with a sharp increase of the exciton size and decrease of the oscillator strength associated with the $S_0 \rightarrow S_3$ transition. After 10 kbar, while the CT character of S_3 continues to increase progressively with pressure (reaching 95% at P = 30 kbar), a close inspection of the electron–hole correlation plots reveals that S_3 gradually evolves towards a charge resonance state. This is further confirmed by both the density variation map and the central position of the CT vector oriented parallel to the CT axis of the molecules. Finally, S_4 initially exhibits a dominant CT character that gradually decreases with increasing pressure, as the exciton becomes more confined. At zero pressure, the charge transfer occurs from monomer **2** to monomer **1** and reverses the direction at P = 10 kbar, after which the transfer occurs from monomer **1** to monomer **2**. Beyond this point, and similar to S_3, S_4 progressively evolves into a charge-resonance state.

Impact of mechanical strain on the nonlinear optical properties

The significant structural changes shown in the previous section to significantly affect the linear optical properties are also expected to strongly influence the NLO response. The evolution with pressure of the static and dynamic components of the first hyperpolarizability vector of the dimer, along with the anisotropy of the NLO response, is summarized in Tables S15 and S16. As in the monomer (Table S17), the β norm (eqn (2)) closely follows that of the β_{zzz} component in both the static and dynamic regimes, confirming that the NLO response is predominantly governed by the diagonal component aligned with the intramolecular charge transfer axis. At P = 0, the static β_{zzz} response of the dimer is roughly twice that of the monomer, albeit slightly lower, as expected for a face-to-face molecular arrangement. In contrast, the monomer and dimer dynamic β_{zzz} responses yield $\beta_{zzz}^{\mathrm{dim}}/2\beta_{zzz}^{\mathrm{mon}} \sim 2.1$, indicating that frequency dispersion effects enhance the NLO response of the aggregated dimer. This enhancement arises from the presence of two highly absorbing excited states, namely, S_2 and S_3, near the second-harmonic wavelength (400 nm, 3.1 eV). As illustrated in Fig. 9, the static and dynamic β responses of the dimer display markedly different behaviours under pressure. The static β decreases progressively as pressure increases and exhibits a sharp discontinuity at 10 kbar, which aligns with the abrupt changes observed in the linear optical properties. Conversely, the dynamic β increases with pressure, reaching a maximum at 9 kbar before decreasing at higher pressures. Notably, the evolution of $\beta(-2\omega;\omega,\omega)$ does not present any clear discontinuity, suggesting that the fine dependence of the SHG response to the nature of the excited states is overridden by frequency dispersion effects. Interestingly, the static anisotropy ratios α_β regularly increase with the pressure, from 25.9 to 43.6, highlighting that the 1D directionality of the NLO response is reinforced by the applied mechanical strain. In contrast, the dynamic anisotropy ratios are lower than the static ones

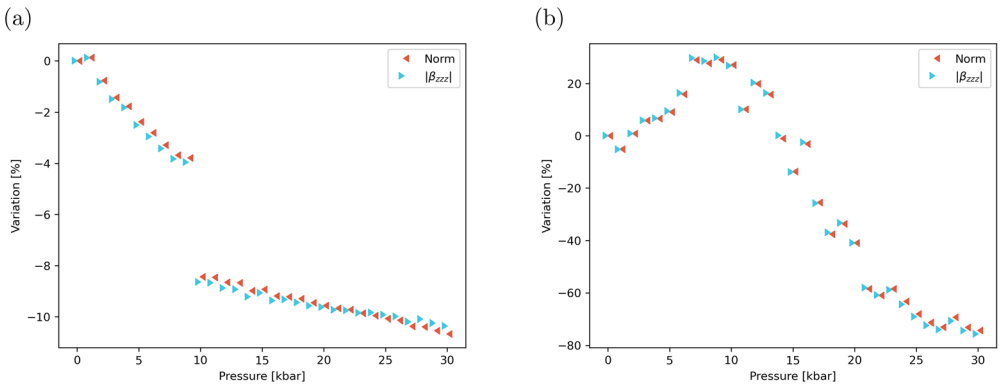

Fig. 9 Pressure-induced variation of the static (a) and dynamic (b) values of β and β_{zzz}, as calculated at the TD-DFT/CAM-B3LYP-D3/6-311G(d) level.

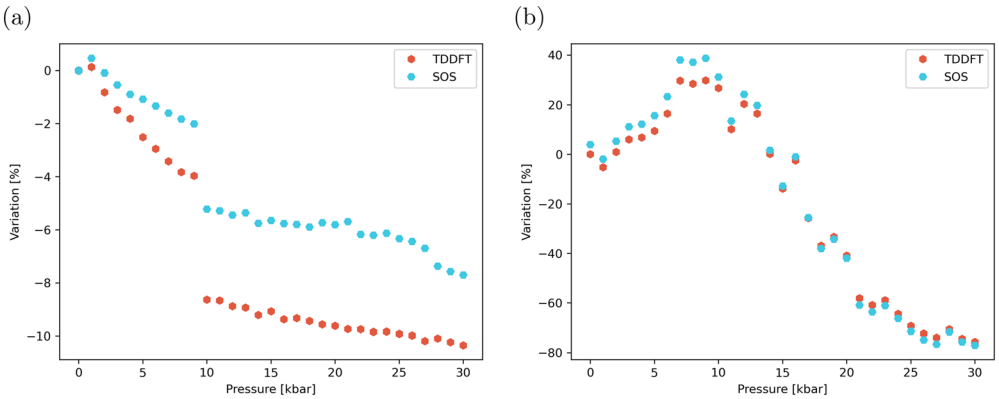

Fig. 10 Pressure-induced evolution (in % variation with respect to the value calculated at zero pressure) of the static (a) and dynamic (b) first hyperpolarizability, as calculated at the TD-DFT/CAM-B3LYP-D3/6-311G(d) level and using the SOS scheme including the first four excited states.

(ranging between 8.7 and 12.1) and display much weaker variations with pressure.

The pressure dependence of β_{zzz} can be further interpreted using the SOS formalism (eqn (4)). In both regimes, the inclusion of only the first four excited states S_1–S_4 is sufficient to reach a converged β_{zzz} value, as shown in Fig. S10. As depicted in Fig. 10, although the β_{zzz} values obtained from the SOS formalism are systematically larger than those computed using TD-DFT, both methods display the same pressure-dependent behaviour.

The SOS formalism also enables the decomposition of the total β_{zzz} component into contributions from individual excited states, as illustrated in Fig. 11. In the static regime, the pressure-induced evolution of the individual state contributions closely mirrors the corresponding changes in their respective oscillator strength. In the dynamic case, however, interpretation of the results is more complex, as the contributions depend both on the intrinsic static response of each state and on frequency-dependent dispersion factors. Among the states considered, S_2 and S_3 provide the largest contributions, owing to their excitation energy ($\Delta E \approx 3.0$–3.2 eV across the pressure range) remaining close to resonance with the 3.1 eV second harmonic light (corresponding to $\lambda = 400$ nm), see Fig. 7. The contribution from S_3 is initially positive (for $\Delta E < 3.1$ eV, up to $\sim$9 kbar), but becomes negative as its excitation energy shifts above the resonance. In contrast, the contribution of S_4 is negligible at low pressures and becomes increasingly negative at higher pressures. Overall, the bell-shape evolution of the dynamic NLO response with pressure shown in Fig. 10 can be largely rationalized by considering only the contribution of the dominant excited state, namely, the contribution of S_3, which increases with pressure between 0 and 9 kbar, and that of S_2, which decreases with pressure in the 9–30 kbar range. However, as illustrated in Fig. 11b, considering only these dominant contributions would result in a discontinuity in the NLO response around 10 kbar. The contribution of S_3, which becomes negative above 9 kbar, smooths out this discontinuity, consistent with the continuous behavior observed in Fig. 10.

Finally, it is worth emphasizing that the pressure dependence of the NLO responses observed for the flexible chromophore studied here contrasts with that computed for more rigid confined structures such as hydrogen-bonded complexes using analytical potential models.[71,72] While those studies concluded that changes in the electronic first hyperpolarizability due to spatial confinement effects are dominated by electron-density compression, with geometry relaxation playing only a minor

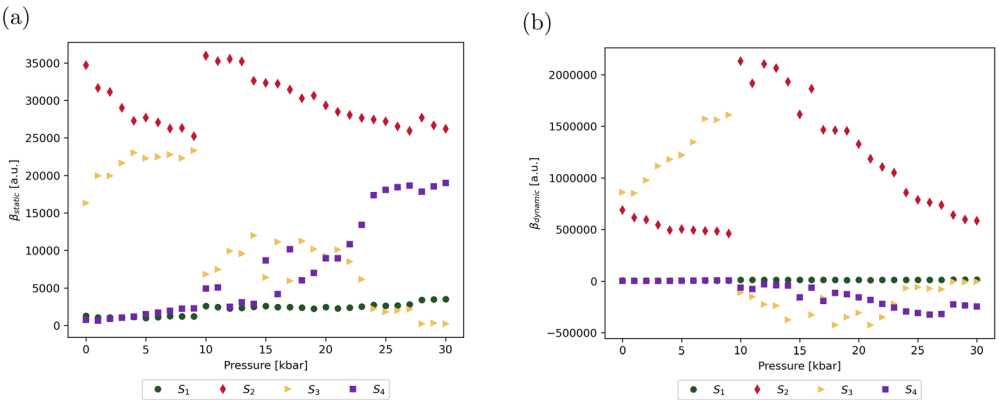

Fig. 11 Contribution of states S_1–S_4 to the static (a) and dynamic (b) β_{zzz} components (a.u.), as calculated using the SOS formalism.

role, the calculations reported in Section 5.1 of the SI reveal a different picture. In the present system, electrostatic interactions with the molecular environment have little effect on the pressure-induced variations of the NLO properties, whereas geometrical distortions, particularly changes in the supramolecular packing and dihedral angles controlling the strength of π-conjugation within the molecules, are identified as the main origin of the large variations observed in the second-order NLO responses. However, as shown in Table S17, electrostatic environment effects induce an 11% reduction of the static first hyperpolarizability at both $P = 0$ and $P = 30$ kbar, while the dynamic first hyperpolarizability increases by 9% and 15% at $P = 0$ and $P = 30$ kbar, respectively, owing to enhanced frequency-resonance effects. Therefore, whereas the calculations reported here correctly capture the trend in the evolution of the NLO response with increasing pressure, an explicit treatment of environmental interactions remains necessary to achieve quantitative accuracy.

Conclusions

In this study, we report a theoretical investigation aiming at rationalizing how external pressure influences the structure and optical properties of a molecular crystal based on the DPA-Th-DCV push–pull chromophore. Periodic DFT optimizations of the crystal structure under increasing isotropic pressure reveal that the applied mechanical strain leads to substantial changes in the unit cell parameters, particularly along the stacking and charge-transfer axes, resulting in a pronounced volume reduction. Pressure also alters key intramolecular torsional angles that directly modulate π-conjugation within the chromophore, as well as intermolecular stacking angles that define the relative orientation of the molecular planes within the crystal. The evolution of these structural parameters is non-monotonic and marked by discontinuities, which are mirrored by abrupt changes in both the energies and oscillator strengths of the low-lying excited states, as calculated on molecular dimers extracted from the optimized crystal structures. Detailed analyses of the first four excited singlets also reveal that pressure-induced structural changes significantly impact the exciton localization and the charge-transfer character of the electronic transitions. Furthermore, TD-DFT calculations indicate that external pressure strongly influences the second harmonic generation response of the dimers, considered representative of the stacking arrangements in thin films. The pressure-induced variation of their SHG response is closely related to the variation of a few set of low-lying excited states, as rationalized using a truncated sum-over-state approach. Overall, these findings suggest that applying external pressure offers a promising route to finely tune the SHG properties of 2D materials based on these push–pull chromophores. Such pressure- and aggregation-induced tunability could be exploited in mechanically responsive nonlinear optical elements, including optical strain or pressure sensors, as well as in adaptive photonic components where the nonlinear response can be modulated by external mechanical constraints. Experimental validation of these theoretical predictions, along with systematic combined theoretical and experimental studies, would be highly valuable for establishing general structure–property relationships and designing new pressure-tunable NLO materials.

Conflicts of interest

There are no conflicts of interest to declare.

Data availability

The data supporting this article have been included as part of the supplementary information (SI). Supplementary information: additional data on (i) the electronic and optical properties of the isolated DPA-Th-DCV molecule, (ii) the pressure-dependent crystal structure properties, (iii) the linear and nonlinear optical properties of the DPA-Th-DCV dimers and (iv) the sum-over-state formalism. Optimized geometries of all systems described in the text are provided in a ZIP archive: (i) geometries of the four stable conformers of the DPA-Th-DCV molecule (pdb format), (ii) pressure-dependent geometries of the crystal unit cell (cif format), and (iii) geometries of the DPA-Th-DCV dimers used in the NLO calculations (pdb format). See DOI: https://doi.org/10.1039/d5cp04030b.

Acknowledgements

We thank Dr J. Roncali and Dr M. Allain for helpful discussions and for providing us with the experimental crystal structures. J. O. thanks the Donostia International Physics Center (DIPC) for her PhD grant. This work was supported by the Transnational Common Laboratory QuantumChemPhys (Theoretical Chemistry and Physics at the Quantum Scale, grant number ANR-10-IDEX-03-02) established between the Université de Bordeaux (UB), Euskal Herriko Unibertsitatea (UPV/EHU) and the DIPC. The authors acknowledge financial support from MCIU/AEI/10.13039/501100011033 (projects PID2022-136231NB-I00 and RED2024-154178-T) and from IKERBASQUE (Basque Foundation for Science). Calculations were performed using the computing facilities provided by the DIPC and the Mésocentre de Calcul Intensif Aquitain (MCIA) of the University of Bordeaux and of the Université de Pau et des Pays de l'Adour.

References

1 W. R. Browne and B. L. Feringa, Light Switching of Molecules on Surfaces, *Annu. Rev. Phys. Chem.*, 2009, **60**, 407–428.
2 C. Wei, X. Lu, X. Wen, Y. Liu and S. Yang, Thermo-responsive color-changeable photonic materials: A review, *Opt. Laser Technol.*, 2022, **152**, 108135.
3 F. Wang, R. Lyu, H. Xu, R. Gong and B. Ding, Tunable colors from responsive 2D materials, *Responsive Mater.*, 2024, **2**, e20240007.

4 J. Jeon, D. Bukharina, M. Kim, S. Kang, J. Kim, Y. Zhang and V. Tsukruk, Tunable and responsive photonic bio-inspired materials and their applications, *Responsive Mater.*, 2024, **2**, e20230032.
5 B. J. Coe, Molecular Materials Possessing Switchable Quadratic Nonlinear Optical Properties, *Chem. – Eur. J.*, 1999, **5**, 2464–2471.
6 J. A. Delaire and K. Nakatani, Linear and Nonlinear Optical Properties of Photochromic Molecules and Materials, *Chem. Rev.*, 2000, **100**, 1817–1846.
7 A. Ségerie, F. Castet, M. B. Kanoun, A. Plaquet, V. Liégeois and B. Champagne, Nonlinear Optical Switching Behavior in the Solid State: A Theoretical Investigation on Anils, *Chem. Mater.*, 2011, **23**, 3993–4001.
8 F. Castet, V. Rodriguez, J. L. Pozzo, L. Ducasse, A. Plaquet and B. Champagne, Design and characterization of molecular nonlinear optical switches, *Acc. Chem. Res.*, 2013, **46**, 2656–2665.
9 M. Schulze, M. Utecht, T. Moldt, D. Przyrembel, C. Gahl, M. Weinelt, P. Saalfrank and P. Tegeder, Nonlinear optical response of photochromic azobenzene-functionalized self-assembled monolayers, *Phys. Chem. Chem. Phys.*, 2015, **17**, 18079–18086.
10 M. Schulze, M. Utecht, A. Hebert, K. Rück-Braun, P. Saalfrank and P. Tegeder, Reversible Photoswitching of the Interfacial Nonlinear Optical Response, *J. Phys. Chem. Lett.*, 2015, **6**, 505–509.
11 C. Tonnelé, B. Champagne, L. Muccioli and F. Castet, Nonlinear Optical Contrast in Azobenzene-Based Self-Assembled Monolayers, *Chem. Mater.*, 2019, **31**, 6759–6769.
12 A. Dellai, L. Muccioli, F. Castet and C. Tonnelé, Second Harmonic Response of Azobenzene Self-Assembled Monolayers: the Effect of Push/Pull Substitution, *J. Phys. Chem. C*, 2025, **129**, 8417–8428.
13 N. Deveaux, F. Mairesse and B. Champagne, Partial Switching in Anil Crystals: Impact on the Second-Order Nonlinear Optical Properties, *J. Phys. Chem. Lett.*, 2025, **16**, 12369–12378.
14 A. Li, J. Wang and Z. Li, Strategies to achieve luminescence enhancement for piezochromic materials under high pressure, *Cell Rep. Phys. Sci.*, 2025, **6**, 102733.
15 S. Nakamura, K. Hirano and N. Tohnai, Organic mechanochromic luminescent materials with self-recovering characters, *ChemPlusChem*, 2024, **89**, e202400437.
16 S. Ito, Recent advances in mechanochromic luminescence of organic crystalline compounds, *Chem. Lett.*, 2021, **50**, 649–660.
17 T. Mutai and S. Takamizawa, Organic soft crystals exhibiting spontaneously reversible mechano-responsive luminescence, *J. Photochem. Photobiol., C*, 2022, **51**, 100479.
18 L. Tu, Y. Xie and Z. Li, Advances in pure organic mechanoluminescence materials, *J. Phys. Chem. Lett.*, 2022, **13**, 5605–5617.
19 Y. Jiang, An outlook review: mechanochromic materials and their potential for biological and healthcare applications, *Mater. Sci. Eng., C*, 2014, **45**, 682–689.
20 V. Kachwal and I. R. Laskar, in *Aggregation-Induced Emission*, ed. Tang Y. and Tang B. Z., Springer International Publishing, 2022, pp. 91–128.
21 C. Lowe and C. Weder, Oligo(p-phenylene vinylene) Excimers as Molecular Probes: Deformation-Induced Color Changes in Photoluminescent Polymer Blends, *Adv. Mater.*, 2002, **14**, 1625–1629.
22 Y. Sagara and T. Kato, Mechanically induced luminescence changes in molecular assemblies, *Nat. Chem.*, 2009, **1**, 605–610.
23 P. Josse, M. Allain, J. P. Calupitan, Y. Jiang, C. Cabanetos and J. Roncali, Structural control of the molecular packing and dynamics of mechanofluorochromic materials based on small donor-acceptor systems with turn-on luminescence, *Adv. Opt. Mater.*, 2020, **8**, 2000420.
24 H. Liu, B. Liu, H. Zhu, J. Bai, H. Zhang and J. Jia, High-contrast mechanofluorochromism of two AIE-active D-A-π-D′ deep red-emitting triphenylamine-based dicyanodiaryl derivatives, *Spectrochim. Acta, Part A*, 2025, **344**, 126666.
25 M. Barłóg, S. K. Podiyanachari, H. S. Bazzi and M. Al-Hashimi, Advances in π-conjugated benzothiazole and benzoxazole-boron complexes: Exploring optical and biomaterial applications, *Macromol. Rapid Commun.*, 2025, **46**, e2400914.
26 S. Tan, J. Tian, S. Yang, B. Zhang, Y. Yang, X. Li and S. Gao, Study on four pyridine-based difluoroboron compounds for mechanofluorochromic behaviors, the ink-free writing and detection of latent fingerprints, *J. Lumin.*, 2024, **275**, 120730.
27 A. Afrin and P. C. A. Swamy, Tailoring emission color shifts in mechanofluorochromic-active AIE systems of carbazole-based D-π-A conjugates: Impact of π spacer unit variants, *J. Org. Chem.*, 2024, **89**, 7946–7961.
28 B. Lu, Y. Zhang, X. Yang, K. Wang, B. Zou and D. Yan, Piezochromic luminescence of AIE-active molecular co-crystals: tunable multiple hydrogen bonding and molecular packing, *J. Mater. Chem. C*, 2018, **6**, 9660–9666.
29 M. Raisch, W. Maftuhin, M. Walter and M. Sommer, A mechanochromic donor–acceptor torsional spring, *Nat. Commun.*, 2021, **12**, 4243.
30 Y. Dong, B. Xu, J. Zhang, X. Tan, L. Wang, J. Chen, H. Lv, S. Wen, B. Li, L. Ye, B. Zou and W. Tian, Piezochromic Luminescence Based on the Molecular Aggregation of 9,10-Bis((E)-2-(pyrid-2-yl)vinyl)anthracene, *Angew. Chem., Int. Ed.*, 2012, **51**(43), 10782–10785.
31 J. Owona, D. Casanova, L. Truflandier, F. Castet and C. Tonnelé, Modelling of pressure-induced charge transfer character in piezoluminescent pyridylvinylanthracene crystals, *J. Mater. Chem. C*, 2024, **12**, 13495–13507.
32 S. Mondal, P. Tanari, S. Roy, S. Bhunia, R. Chowdhury, A. K. Pal, A. Datta, B. Pal and C. M. Reddy, Autonomous self-healing organic crystals for nonlinear optics, *Nat. Commun.*, 2023, **14**, 6589.
33 J. Lin, J. Zhou, Z. Wang, L. Li, M. Li, J. Xu, S. Wu, P. Naumov and J. Gong, Low-Temperature Flexibility of Chiral Organic Crystals with Highly Efficient Second-Harmonic Generation, *Angew. Chem., Int. Ed.*, 2025, **64**, e202416856.

34 J. Lin, S. Tang, L. Li, L. Fang, Q. Zeng, G. Sun, S. Wu, P. Naumov and J. Gong, Flexible Organic Crystalline Fibers and Loops with Strong Second Harmonic Generation, *J. Am. Chem. Soc.*, 2025, **147**(13), 11346–11358.
35 Z. Wang, W. Han, B. Fu, H. Kang, P. Cheng, J. Guan, Y. Zheng, R. Shi, J. Xu and X.-H. Bu, Mechanical Twisting-Induced Enhancement of Second-Order Optical Nonlinearity in a Flexible Molecular Crystal, *J. Am. Chem. Soc.*, 2025, **147**, 2766–2775.
36 G. Yang, Z. A. Dreger and H. G. Drickamer, High-pressure studies of second harmonic generation in organic materials, *Chem. Phys. Lett.*, 1997, **280**, 375–380.
37 Y. Li, G. Yang, Z. A. Dreger, J. O. White and H. G. Drickamer, Effect of high pressure on the second harmonic generation efficiencies of three monoclinic organic compounds, *J. Phys. Chem. B*, 1998, **102**, 3032–3038.
38 W. Cai, J. He, W. Li and A. Katrusiak, Anomalous compression of a weakly CHO bonded nonlinear optical molecular crystal, *J. Mater. Chem. C*, 2014, **2**, 6471–6476.
39 G. de Moura, S. A. de Azevedo, J. R. Sambrano, M. Lage, A. D. Santos, S. Stoyanov and T. Andrade-Filho, Optical properties of sarcosine crystal under hydrostatic pressure: a DFT-based computational study, *Phys. Chem. Chem. Phys.*, 2025, **27**, 14042–14053.
40 Y. Mao, S. Guo, X. Huang, K. Bu, Z. Li, P. Q. H. Nguyen, G. Liu, Q. Hu, D. Zhang, Y. Fu, W. Yang and X. Lü, Pressure-Modulated Anomalous Organic–Inorganic Interactions Enhance Structural Distortion and Second-Harmonic Generation in MHyPbBr3 Perovskite, *J. Am. Chem. Soc.*, 2023, **145**, 23842–23848.
41 V. Tsukanova, A. Harata and T. Ogawa, Second-Harmonic Probe of Pressure-Induced Structure Ordering within Long-Chain Fluorescein Monolayer at the Air/Water Interface, *J. Phys. Chem. B*, 2000, **104**, 7707–7712.
42 Y. Jiang, D. Gindre, M. Allain, P. Liu, C. Cabanetos and J. Roncali, A mechanofluorochromic push-pull small molecule with aggregation-controlled linear and nonlinear optical properties, *Adv. Mater.*, 2015, **27**, 4285–4289.
43 M. J. Frisch, *et al. Gaussian 16, Revision B.01*, Gaussian Inc., Wallingford CT, 2016.
44 T. Yanai, D. P. Tew and N. C. Handy, A new hybrid exchange-correlation functional using the Coulomb-attenuating method (CAM-B3LYP), *Chem. Phys. Lett.*, 2004, **393**, 51–57.
45 S. Grimme, J. Antony, S. Ehrlich and H. Krieg, A consistent and accurate ab initio parametrization of density functional dispersion correction (DFT-D) for the 94 elements H-Pu, *J. Chem. Phys.*, 2010, **132**, 154104.
46 J. Tomasi, B. Mennucci and R. Cammi, Quantum mechanical continuum solvation models, *Chem. Rev.*, 2005, **105**, 2999–3093.
47 P. Giannozzi, *et al.*, QUANTUM ESPRESSO: a modular and open-source software project for quantum simulations of materials, *J. Phys.:Condens. Matter*, 2009, **21**, 395502.
48 P. Giannozzi, *et al.*, QUANTUM ESPRESSO: a modular and open-source software project for quantum simulations of materials, *J. Phys.:Condens. Matter*, 2017, **29**, 465901.
49 V. R. Cooper, van der Waals density functional: An appropriate exchange functional, *Phys. Rev. B: Condens. Matter Mater. Phys.*, 2010, **81**, 161104.
50 D. C. Langreth, *et al.*, A density functional for sparse matter, *J. Phys.:Condens. Matter*, 2009, **21**, 084203.
51 K. Berland, V. R. Cooper, K. Lee, E. Schröder, T. Thonhauser, P. Hyldgaard and B. I. Lundqvist, van der Waals forces in density functional theory: a review of the vdW-DF method, *Rep. Prog. Phys.*, 2015, **78**, 066501.
52 G. Prandini, A. Marrazzo, I. E. Castelli, N. Mounet, E. Passaro and N. Marzari, A Standard Solid State Pseudopotentials (SSSP) library optimized for precision and efficiency, *Mater. Cloud Arch.*, 2021, **2021**, 76.
53 G. Prandini, A. Marrazzo, I. E. Castelli, N. Mounet and N. Marzari, Precision and efficiency in solid-state pseudopotential calculations, *npj Comput. Mater.*, 2018, **4**, 72.
54 K. Lejaeghere, *et al.*, Reproducibility in density functional theory calculations of solids, *Science*, 2016, **351**, 1415.
55 A. H. Larsen, *et al.*, The atomic simulation environment—a Python library for working with atoms, *J. Phys.: Condens. Matter*, 2017, **29**, 273002.
56 C. F. Macrae, I. Sovago, S. J. Cottrell, P. T. A. Galek, P. McCabe, E. Pidcock, M. Platings, G. P. Shields, J. S. Stevens, M. Towler and P. A. Wood, Mercury 4.0: from visualization to analysis, design and prediction, *J. Appl. Crystallogr.*, 2020, **53**, 226–235.
57 K. Momma and F. Izumi, VESTA 3 for three-dimensional visualization of crystal, volumetric and morphology data, *J. Appl. Crystallogr.*, 2011, **44**, 1272–1276.
58 F. Plasser, TheoDORE: A toolbox for a detailed and automated analysis of electronic excited state computations, *J. Chem. Phys.*, 2020, **152**, 084108.
59 B. J. Orr and J. F. Ward, Perturbation theory of the nonlinear optical polarization of an isolated system, *Mol. Phys.*, 1971, **20**, 513–526.
60 K. Sasagane, F. Aiga and R. Itoh, Higher-order response theory based on the quasienergy derivatives: The derivation of the frequency-dependent polarizabilities and hyperpolarizabilities, *J. Chem. Phys.*, 1993, **99**, 3738–3778.
61 D. M. Bishop, Explicit nondivergent formulas for atomic and molecular dynamic hyperpolarizabilities, *J. Chem. Phys.*, 1994, **100**, 6535–6542.
62 T. Lu and F. W. Chen, Multiwfn: a multifunctional wavefunction analyzer, *J. Comput. Chem.*, 2012, **33**, 580–592.
63 T. Lu and F. W. Chen, Calculation of molecular orbital composition, *Acta Chim. Sin.*, 2011, **69**, 2393–2406.
64 H. Reis, Problems in the comparison of theoretical and experimental hyperpolarizabilities revisited, *J. Chem. Phys.*, 2006, **125**, 014506.
65 L. W. Chung, W. M. C. Sameera, R. Ramozzi, A. J. Page, M. Hatanaka, G. P. Petrova, T. V. Harris, X. Li, Z. Ke, F. Liu, H.-B. Li, L. Ding and K. Morokuma, The ONIOM Method and Its Applications, *Chem. Rev.*, 2015, **115**, 5678–5796.
66 A. Tuer, S. Krouglov, R. Cisek, D. Tokarz and V. Barzda, Three-dimensional visualization of the first hyperpolarizability tensor, *J. Comput. Chem.*, 2011, **32**, 1128–1134.

67 E. R. Johnson, S. Keinan, P. Mori-Sánchez, J. Contreras-García, A. J. Cohen and W. Yang, Revealing noncovalent interactions, *J. Am. Chem. Soc.*, 2010, **132**, 6498–6506.

68 J. Contreras-García, E. R. Johnson, S. Keinan, R. Chaudret, J. P. Piquemal, D. N. Beratan and W. Yang, NCIPLOT: a program for plotting noncovalent interaction regions, *J. Chem. Theory Comput.*, 2011, **7**, 625–632.

69 T. L. Bahers, C. Adamo and I. Ciofini, A qualitative index of spatial extent in charge-transfer excitations, *J. Chem. Theory Comput.*, 2011, **7**, 2498–2506.

70 D. Jacquemin, T. L. Bahers, C. Adamo and I. Ciofini, What is the 'best' atomic charge model to describe through-space charge-transfer excitations?, *Phys. Chem. Chem. Phys.*, 2012, **14**, 5383–5388.

71 R. Zaleśny, M. Chołuj, J. Kozłowska, W. Bartkowiak and J. M. Luis, Vibrational nonlinear optical properties of spatially confined weakly bound complexes, *Phys. Chem. Chem. Phys.*, 2017, **19**, 24276–24283.

72 A. Iglesias-Reguant, R. Zaleśny and J. M. Luis, Nonlinear optical properties and intermolecular interactions, *Coord. Chem. Rev.*, 2026, **553**, 217566.

